

## PERFECTLY MATCHED LAYER BOUNDARY INTEGRAL EQUATION METHOD FOR WAVE SCATTERING IN A LAYERED MEDIUM\*

WANGTAO LU<sup>†</sup>, YA YAN LU<sup>‡</sup>, AND JIANLIANG QIAN<sup>§</sup>

**Abstract.** For scattering problems of time-harmonic waves, the boundary integral equation (BIE) methods are highly competitive since they are formulated on lower-dimension boundaries or interfaces and can automatically satisfy outgoing radiation conditions. For scattering problems in a layered medium, standard BIE methods based on Green's function of the background medium need to evaluate the expensive Sommerfeld integrals. Alternative BIE methods based on the free-space Green's function give rise to integral equations on unbounded interfaces which are not easy to truncate since the wave fields on these interfaces decay very slowly. We develop a BIE method based on the perfectly matched layer (PML) technique. The PMLs are widely used to suppress outgoing waves in numerical methods that directly discretize the physical space. Our PML-based BIE method uses the PML-transformed free-space Green's function to define the boundary integral operators. The method is efficient since the PML-transformed free-space Green's function is easy to evaluate and the PMLs are very effective in truncating the unbounded interfaces. Numerical examples are presented to validate our method and demonstrate its accuracy.

**Key words.** boundary integral equation, perfectly matched layer, scattering problem, Neumann-to-Dirichlet map

**AMS subject classifications.** 65R20, 78A40, 31A10

**DOI.** 10.1137/17M1112510

**1. Introduction.** Scattering problems for sound, electromagnetic, and elastic waves in layered media are highly relevant for practical applications [11]. Numerical methods that directly discretize the physical domain, such as the finite element method (FEM) [26], are versatile and widely used, but they become too expensive when the scatterer is large compared with the wavelength. The boundary integral equation (BIE) methods [13] are applicable to structures with piecewise constant material parameters. These methods take care of the outgoing radiation condition automatically and reduce the dimension by one since the integral equations are formulated on material interfaces or boundaries of obstacles. For many problems, BIE methods can outperform FEM and other domain-discretization methods and deliver highly accurate solutions with relatively reasonable computing effort.

For scattering problems in a layered medium, the common BIE methods are based on Green's function of the layered background medium [32, 34, 39] so that the integral equations are formulated on strictly local interfaces or boundaries. However, it is

---

\*Received by the editors January 20, 2017; accepted for publication (in revised form) September 29, 2017; published electronically January 24, 2018.

<http://www.siam.org/journals/siap/78-1/M111251.html>

**Funding:** The first author's work was partially supported by the Hundred Talents Program of Zhejiang University and by the National Thousand Young Talents Program, China. The second author's work was partially supported by the Research Grants Council of Hong Kong Special Administrative Region, China (Grant No. CityU 11301914). The third author's work was partially supported by NSF grants 1522249 and 1614566.

<sup>†</sup>School of Mathematical Sciences, Zhejiang University, Hangzhou, Zhejiang 310027, China (wangtaolu@zju.edu.cn).

<sup>‡</sup>Department of Mathematics, City University of Hong Kong, Kowloon, Hong Kong (mayylu@cityu.edu.hk).

<sup>§</sup>Department of Mathematics, Michigan State University, East Lansing, MI 48824 (qian@math.msu.edu).

well known that this approach is bottlenecked by the evaluation of Sommerfeld integrals arising from the layered-medium Green's function and its derivatives. Over the past decades, many methods, such as high-frequency asymptotics, rational approximations, contour deformations [7, 8, 29, 30, 31], complex images [28, 36, 37], and the steepest descent method [14, 15], have been developed to speed up the computation of Sommerfeld integrals. A detailed discussion on computational cost for evaluating the Sommerfeld integrals can be found in [6].

An alternative approach is to use the free-space Green's function, but then the integral equations must also be formulated on the unbounded interfaces separating different layers of the background medium. Various types of compactly supported functions can be used to truncate the unbounded interfaces and to suppress the artificial reflections from the edges of the truncated sections. Existing methods in this category include the approximate truncation method [24, 33], the taper function method [40, 35, 25], and the windowing function method [4, 27, 5, 20]. In particular, the windowing function method [5] can largely eliminate the artificial reflections since the errors decrease superalgebraically as the window size is increased. Similar good performance can be observed in [20] that combines windowed layer potentials (in physical space) with a Sommerfeld-type correction (in Fourier space) for scattering problems where the obstacles are close to or even cut through the interfaces of the background layered medium.

In this paper, we develop a BIE method based on perfectly matched layers (PMLs) for two-dimensional (2D) scattering problems in layered media. The PML technique is widely used for domain truncations in wave propagation problems [3, 12]. It can be regarded as a complex coordinate stretching that replaces real independent variables in the original governing equation by complex independent variables so that the outgoing waves are damped as they propagate into the PML region. Similar to those BIE methods based on the free-space Green's function, our BIE method avoids evaluating expensive Sommerfeld integrals by formulating integral equations along the interfaces of the background layered medium. But instead of the free-space Green's function, we use the PML-transformed free-space Green's function so that the truncation of the interfaces follows automatically from the truncation of PMLs. Notice that the PML-transformed free-space Green's function can be simply obtained by extending the argument of the usual Green's function to complex space following the definition of the complex square root function.

We implement our PML-based BIE method for 2D scattering problems involving two homogeneous media separated by a single interface. The interface is flat except in a finite section which is referred to as the local perturbation. Additional obstacles are also allowed in the homogeneous media. Two common types of incident waves are considered: a plane incident wave and a cylindrical wave due to a point source. The integral equations are established for a scattered wave satisfying the following radiation condition at infinity: The scattered wave consists of outgoing plane waves and evanescent waves [17, 9, 2]. The scattered wave is defined as the difference between the total wave field and a reference wave field obtained from the same incident wave for the layered background medium (without the local perturbation of the interface and the obstacles).

BIE methods for scattering problems use many different formulations. Some of these formulations are more appropriate for large (i.e., high-frequency) problems since they give rise to linear systems with better condition numbers which are amenable to iterative methods. Since our purpose is to demonstrate the effectiveness of PML-based BIEs for truncating unbounded interfaces, we adopt a BIE formulation that comes

from Green's representation theorem directly. In addition, we calculate the so-called Neumann-to-Dirichlet (NtD) map (mapping Neumann data to Dirichlet data on the boundary) for each subdomain with constant material parameters so that the final linear system on interfaces or boundaries of the obstacles can be written down in a very simple form.

To numerically approximate the integral equations, we utilize a graded mesh technique [13], a high-order quadrature rule by Alpert [1], and a novel stabilizing technique. Numerical results indicate that our method is highly accurate and the truncation of the unbounded interfaces by PML is effective. Typically, for a PML with a thickness of one wavelength and discretized in the same way as discretizing physical space, about seven significant digits can be obtained. Numerical results indicate that if the error is dominated by the truncation of the domain, it decays exponentially when the strength of the PML is increased.

The rest of this paper is organized as follows. In sections 2 and 3, we present our PML-based BIE formulation for solving scattering problems in a layered media. Numerical schemes for discretizing the integral equations are given in section 4. Numerical examples are presented in section 5 to illustrate the performance of our method, and we conclude the paper in section 6.

**2. Problem formulation.** We focus on layered-medium scattering problems in two dimensions. As shown in Figure 1, the layered medium is  $x_3$ -invariant and consists of two homogeneous Lipschitz domains  $\Omega_1$  and  $\Omega_2$  with constant refractive index  $n_1$  and  $n_2$ , respectively. The interface  $\Gamma$  on  $x_2 = 0$  separates  $\Omega_1$  and  $\Omega_2$  and contains a local perturbation curve  $P$ . Throughout this paper, we assume that the Lipschitz boundary  $\Gamma$  is piecewise analytic and contains a finite number of corners. Here,  $(x_1, x_2, x_3)$  denotes the standard Cartesian coordinate system.

Let  $u^{inc}$  be an incident wave from the upper medium  $\Omega_1$ . The total wave field  $u^{tot}$ , representing the  $x_3$ -component of the electric field in the TE polarization or the  $x_3$ -component of the magnetic field in the TM polarization, solves

$$(1) \quad \Delta u^{tot} + k_0^2 n_j^2 u^{tot} = 0 \quad \text{in } \Omega_j$$

$$(2) \quad [u^{tot}] = 0, \quad \left[ \frac{\eta_j \partial u^{tot}}{\partial \nu} \right] = 0 \quad \text{on } \Gamma$$

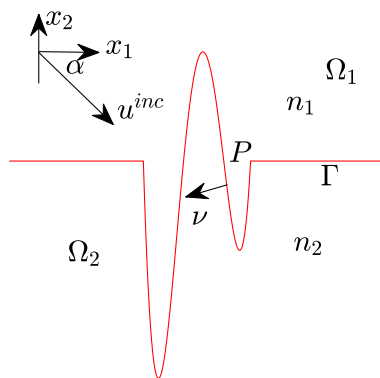


FIG. 1. Profile of a 2D layered medium.

where  $k_0 = \frac{2\pi}{\lambda}$  is the free-space wavenumber,  $\lambda$  is the wavelength,  $\nu$  denotes the unit normal vector along  $\Gamma$  pointing toward  $\Omega_2$ ,  $[f]$  denotes the jump of the quantity  $f$  across  $\Gamma$ ,  $\eta_j = 1$  in the TE polarization, and  $\eta_j = \frac{1}{n_j^2}$  in the TM polarization.

In this paper, we consider two cases of incident waves: a plane wave and a cylindrical wave due to a source at  $x^* = (x_1^*, x_2^*) \in \Omega_1$ . In the latter case, equation (1) should be replaced by

$$(3) \quad \Delta u^{tot} + k_0^2 n_j^2 u^{tot} = -\delta(x, x^*) \quad \text{in } \Omega_j$$

so that  $u^{tot}$  represents the layered-medium Green's function excited by the source at  $x^*$ . Our scattering problem is to solve (1) and (2) for  $u^{tot}$ , subject to the following radiation condition at infinity:  $u^{tot}$  is the sum of a known reference wave field  $u_0^{tot}$  and a scattered wave field  $u^s := u^{tot} - u_0^{tot}$  that consists of outgoing plane waves and evanescent plane waves both above and below  $\Gamma$ ; see the angular spectrum representation [17] and also the equivalent upward propagating radiation condition [9, 2].

For the case of plane incident waves, suppose  $u^{inc} = e^{ik_0 n_1 (x_1 \cos \alpha - x_2 \sin \alpha)}$ , where  $\alpha \in (0, \pi)$  denotes the angle between the wave direction and the positive  $x_1$ -axis. The reference wave field  $u_0^{tot}$  is the solution to the scattering problem with the flat interface  $x_2 = 0$  and with the same incident wave  $u^{inc}$ . It is easy to get that

$$(4) \quad u_0^{tot} = \begin{cases} e^{ik_0 n_1 (x_1 \cos \alpha - x_2 \sin \alpha)} + R e^{ik_0 n_1 (x_1 \cos \alpha + x_2 \sin \alpha)} & \text{in } \Omega_1, \\ (R + 1) e^{ik_0 n_1 x_1 \cos \alpha - ik^* x_2} & \text{in } \Omega_2, \end{cases}$$

where

$$k^* = k_0 \sqrt{n_2^2 - n_1^2 \cos^2 \alpha},$$

$$R = \frac{2}{1 + \frac{k^* \eta}{k_0 n_1 \sin \alpha}} - 1,$$

and  $\eta = \eta_1/\eta_2$ ; when  $n_2 \leq |n_1 \cos \alpha|$ , we set  $k^* = ik_0 \sqrt{n_1^2 \cos^2 \alpha - n_2^2}$ . On the other hand, if the incident wave is  $u^{inc} = \frac{i}{4} H_0^{(1)}(k_0 n_1 |x - x^*|)$ , a cylindrical wave excited by  $x^* \in \Omega_1$ , then

$$(5) \quad u_0^{tot} = \begin{cases} u^{inc}, & \text{in } \Omega_1, \\ 0, & \text{in } \Omega_2. \end{cases}$$

Instead of directly computing  $u^{tot}$ , we choose to compute the scattered wave field  $u^s$ , which satisfies the following transmission condition:

$$(6) \quad u_1^s|_\Gamma - u_2^s|_\Gamma = -[u_0^{tot}]$$

$$(7) \quad \eta_1 \frac{\partial u_1^s}{\partial \nu} \Big|_\Gamma - \eta_2 \frac{\partial u_2^s}{\partial \nu} \Big|_\Gamma = - \left[ \eta_j \frac{\partial u_0^{tot}}{\partial \nu} \right]$$

where  $u_j^s$  denotes  $u^s$  in  $\Omega_j$  for  $j = 1, 2$ . Note that outside the perturbation curve  $P$ ,  $[u_0^{tot}]$  and  $[\eta_j \partial_\nu u_0^{tot}]$  become zero for plane waves, but they are nonzero for cylindrical waves.

In a typical BIE formulation, computing  $u^s$  in the  $x_1 x_2$ -plane can be reduced to computing  $u_j^s$  and  $\partial_\nu u_j^s$  on the interface  $\Gamma$  only. To solve the governing equations (6) and (7), we require further relations between  $u_j^s$  and  $\partial_\nu u_j^s$  for  $j = 1, 2$ . Suppose

that under certain regularity condition, the NtD map  $\mathcal{N}_j$ , mapping  $\partial_\nu u_j^s$  to  $u_j^s$  on the interface  $\Gamma$ , exists; then, (6) and (7) become

$$(8) \quad \begin{bmatrix} \mathcal{N}_1 & -\mathcal{N}_2 \\ \eta_1 \mathcal{I} & -\eta_2 \mathcal{I} \end{bmatrix} \begin{bmatrix} \partial_\nu u_1^s|_\Gamma \\ \partial_\nu u_2^s|_\Gamma \end{bmatrix} = \begin{bmatrix} -[u_0^{tot}] \\ -[\eta_j \partial_\nu u_0^{tot}] \end{bmatrix},$$

where  $\mathcal{I}$  denotes the identity operator. If the operator matrix on the left-hand side of (8) is invertible, we obtain  $\partial_\nu u_j^s|_\Gamma$  and then  $u_j^s|_\Gamma = \mathcal{N}_s^j \partial_\nu u_j^s|_\Gamma$ .

In the following, we present a PML-based BIE formulation to solve the problem (8) after a truncation of  $\Gamma$ .

**3. NtD map on interface of a PML truncation.** Without loss of generality, we consider only the upper homogeneous domain  $\Omega_1$ , and we will suppress the subscript 1 indexing the domain  $\Omega_1$  so that we use  $\Omega$ ,  $u^s$ , and  $n$  to denote  $\Omega_1$ ,  $u_1^s$ , and  $n_1$ , respectively.

**3.1. Direct truncation.** As shown in Figure 2(a), we place a box bounded by  $\Gamma^+ \cup \Gamma^-$  to enclose  $P$  and to truncate the  $x_1x_2$ -plane. Then the interface  $\Gamma$  is truncated to  $\Gamma_{AB} = AP_L \cup P \cup P_RB$ , while  $\Omega$  is truncated to a bounded domain  $\Omega^b$  with the boundary  $\Gamma^b = \Gamma_{AB} \cup \Gamma^+$ . Existing integral operator theories give the following proposition.

PROPOSITION 3.1. *In the bounded Lipschitz domain  $\Omega^b$ , we have the following:*

(a) *Let  $g \in H^{-1/2+\delta}(\Gamma^b)$  for  $0 < \delta < 1/2$ . If  $u^s \in H^{1+\delta}(\Omega^b) (\subset C^{0,\delta}(\overline{\Omega^b}))$ , a Hölder continuous function of order  $\delta$ ) solves*

$$(9) \quad \begin{cases} \Delta u^s + k_0^2 n^2 u^s = 0 & \text{in } \Omega^b, \\ \partial_\nu u^s = g & \text{on } \Gamma^b, \end{cases}$$

where  $\nu$  denotes the exterior unit normal vector, we have the following representation formula:

$$(10) \quad u^s(x) = \int_{\Gamma^b} \{G(x, y) \partial_\nu u^s(y) - \partial_\nu G(x, y) u^s(y)\} ds(y)$$

for  $x \in \Omega^b$ , where  $G(x, y) = \frac{i}{4} H_0^{(1)}(k_0 n |x - y|)$  is Green's function of the Helmholtz equation in (9). As  $x$  approaches  $\Gamma^b$ , (10) becomes

$$(11) \quad (\mathcal{K} + \mathcal{I})(u^s)(x) = \mathcal{S}(\partial_\nu u^s)(x)$$

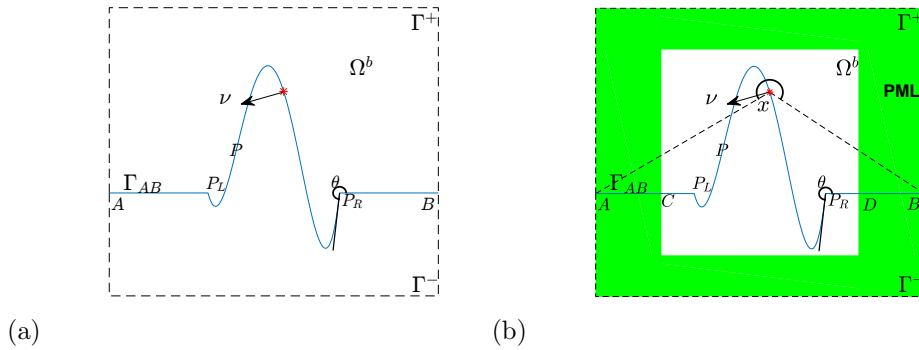


FIG. 2. Two truncation approaches: (a) direct truncation and (b) PML truncation.

for a.e.  $x \in \Gamma^b$ , where the boundary integral operators  $\mathcal{K}$  and  $\mathcal{S}$  are defined as

$$(12) \quad \mathcal{S}(\phi)(x) = 2 \int_{\Gamma^b} G(x, y)\phi(y)ds(y)$$

$$(13) \quad \mathcal{K}(\phi)(x) = 2 \int_{\Gamma^b} \partial_{\nu} G(x, y)\phi(y)ds(y)$$

and  $\int$  denotes the Cauchy principal integral.

(b) The operator  $\mathcal{K} + \mathcal{I}: H^{1/2+\delta}(\Gamma^b) \rightarrow H^{1/2+\delta}(\Gamma^b)$  is Fredholm of index zero.

*Proof.*

(a). Equation (10) follows from Theorem 7.7 in [23, p. 229]. Equation (11) follows from the jumping conditions in equation (7.5) in [23, p. 218].

(b). We now consider the operator

$$\mathcal{K} + \mathcal{I} = \mathcal{K} - \mathcal{K}_0 + \mathcal{K}_0 + \mathcal{I},$$

where we define

$$(14) \quad \mathcal{K}_0(\phi)(x) = 2 \int_{\Gamma^b} \partial_{\nu} G_0(x, y)\phi(y)ds(y)$$

and  $G_0(x, y) = \frac{1}{2\pi} \log|x - y|$  is Green's function of Laplace operator  $-\Delta$ . Since  $\mathcal{K} - \mathcal{K}_0$  is compact from  $H^0(\Gamma^b)$  to  $H^1(\Gamma^b)$  [16, Theorem 4.3], we see from Theorem 3.27 in [23, p. 87] that  $\mathcal{K} - \mathcal{K}_0$  is compact from  $H^{1/2+\delta}(\Gamma^b)$  to  $H^{1/2+\delta}(\Gamma^b)$ . Consequently, (b) follows from the fact that  $\mathcal{K}_0 + \mathcal{I}: H^{1/2+\delta}(\Gamma^b) \rightarrow H^{1/2+\delta}(\Gamma^b)$  is Fredholm of index zero [16, Theorem 4.4].  $\square$

According to Proposition 3.1, if  $k_0^2 n^2$  is not an eigenvalue of problem (9) with  $g \equiv 0$  on  $\Gamma^b$ , then  $\mathcal{K} + \mathcal{I}: H^{1/2+\delta}(\Gamma^b) \rightarrow H^{1/2+\delta}(\Gamma^b)$  is invertible so that the NtD map  $\mathcal{N} = (\mathcal{K} + \mathcal{I})^{-1}\mathcal{S}$  mapping from Neumann data  $\partial_{\nu} u \in H^{-1/2+\delta}(\Gamma^b)$  to Dirichlet data  $u \in H^{1/2+\delta}(\Gamma^b)$  exists.

According to [19, equation (6.50)], equation (11) does not hold at the finite number of corners of  $\Gamma^b$  and should be modified to

$$(15) \quad \mathcal{K}(u^s)(x) + \frac{\theta(x)}{\pi} u^s(x) = \mathcal{S}(\partial_{\nu} u^s)(x)$$

so that it holds for all  $x \in \Gamma^b$ . Here,  $\theta(x)$  is defined as the interior angle between the left and right tangents of  $x$  on  $\Gamma^b$  that is inside  $\Omega^b$ ; see  $\theta(P_R)$  in Figure 2. Moreover, if we set  $\phi \equiv 1$  in equation (6.50) in [19], we obtain

$$(16) \quad \mathcal{K}_0(1)(x) = -\frac{\theta(x)}{\pi}$$

for all  $x \in \Gamma^b$ . Hence, equation (15) can be rewritten as

$$(17) \quad [\mathcal{K} - \mathcal{K}_0(1)](u^s) = \mathcal{S}(\partial_{\nu} u^s)$$

on  $\Gamma^b$ . In practice, as suggested in [18, p. 158] and in [13, section 3.5],  $\mathcal{K}_0(1)$  must be numerically evaluated based on the same discretization as for  $\mathcal{K}$ ; directly using its exact value (16) causes pronounced numerical errors in the vicinity of corners which was verified in [22, section 6]. Consequently, we prefer defining the NtD map  $\mathcal{N} = [\mathcal{K} - \mathcal{K}_0(1)]^{-1}\mathcal{S}$ .

To truncate  $\mathcal{N}$  onto  $\Gamma_{AB}$  only, a significant question arises: What boundary conditions should we impose on  $\Gamma^+$ ? One may directly specify that  $u^s \approx 0$  and  $\partial_\nu u^s \approx 0$  on  $\Gamma^+$ , but this induces a large truncation error as illustrated in [17, section IV]. Certainly, we may place  $\Gamma^+$  farther away from  $P$  to reduce the truncation error, but this increases the computational burden. To maintain computational efficiency and to reduce the truncation error, we design a PML to make  $u^s$  and  $\partial_\nu u^s$  decay more rapidly, as will be presented below.

**3.2. PML truncation.** We introduce the complex coordinate stretching function  $\tilde{x}(x) = (\tilde{x}_1(x_1), \tilde{x}_2(x_2))$  by defining

$$(18) \quad \tilde{x}_l(x_l) = x_l + i \int_0^{x_l} \sigma_l(t) dt$$

for  $l = 1, 2$ , where we take

$$(19) \quad \sigma_l(t) = \sigma_l(-t), \sigma_l = 0 \text{ for } |t| \leq a_l \text{ and } \sigma_l(t) > 0 \text{ for } |t| > a_l$$

and  $a_1, a_2 > 0$  are such that  $[-a_1, a_1] \times [-a_2, a_2]$  encloses the perturbation curve  $P$ . Domains with nonzero  $\sigma_l$  are called the *perfectly matched layer* (PML) [3, 12]; see the shaded region shown in Figure 2(b). Then we choose  $[-a_1 - T, a_1 + T] \times [-a_2 - T, a_2 + T]$  as the box in the previous section to truncate the  $x_1x_2$ -plane, where  $T > 0$  denotes the thickness of the PML in  $\Omega^b$ .

In principle,  $\sigma_l$  can be any positive function in the PML region for  $|t| > a_l$ , e.g., a constant function used in [10]. However, discontinuities of  $\sigma_j$  lead to artificial corners on  $\Gamma_{AB}$  which are not preferred in our BIE formulation since otherwise the mesh points to be constructed on  $\Gamma_{AB}$  will partly cluster at  $|t| = a_l$ , which brings in an unnecessary risk of numerical instability, as will be illustrated in section 4.2. Thus, we enforce  $\sigma_j$  being sufficiently smooth in the domain  $\Omega^b$ . Taking  $\sigma_1$  as an example, its derivatives should vanish at  $C$  and  $D$  up to a desired order; here, we make use of a scaling function, similar to the function  $w$  in [13, equation (3.104)], to define  $\sigma_1$ . Specifically, we take

$$(20) \quad \sigma_1(x_1) = \begin{cases} \frac{2Sf_1^p}{f_1^p + f_2^p}, & a_1 \leq x_1 \leq a_1 + T, \\ S, & x_1 > a_1 + T, \\ \sigma_1(-x_1), & x_1 \leq -a_1, \end{cases}$$

where  $p$  is a positive integer,

$$f_1 = \left(\frac{1}{2} - \frac{1}{p}\right) \bar{x}_1^3 + \frac{\bar{x}_1}{p} + \frac{1}{2}, \quad f_2 = 1 - f_1, \quad \bar{x}_1 = \frac{x_1 - (a_1 + T)}{T},$$

and  $S > 0$  determines the magnitude of  $\sigma_1$  so that it can be used to adjust the PML strength for absorbing a scattered wave [12]. It is not hard to show that  $\sigma_1$  maps  $[a_1, a_1 + T]$  onto  $[0, S]$  and its derivatives vanish at  $x_1 = \pm a_1$  up to order  $p$ . Figure 3 displays the graph of  $\sigma_1(x_1)$  used in Example 1 of section 5, where we set  $a_1 = T = 1$ ,  $S = 2$ , and  $p = 6$ . One similarly defines  $\sigma_2$ .

Using Green’s representation formula (10), we can analytically continue  $u^s$  in the domain  $\tilde{\Omega}^b = \{\tilde{x}(x) | x \in \Omega^b\}$  by defining for  $\tilde{x} \in \tilde{\Omega}^b$

$$(21) \quad u^s(\tilde{x}) = \int_{\Gamma^b} \{G(\tilde{x}, y) \partial_\nu u^s(y) - \partial_\nu G(\tilde{x}, y) u^s(y)\} dy.$$

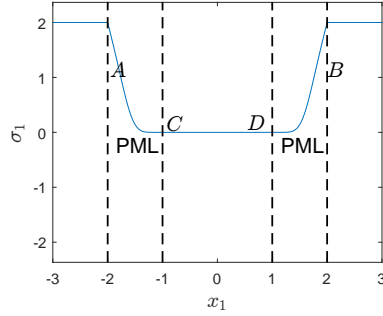


FIG. 3. A typical profile of  $\sigma_1$ .

According to [21, Lemma 2.3],  $u^s(\tilde{x})$  satisfies

$$(22) \quad \tilde{\Delta} u^s(\tilde{x}) + k_0^2 n^2 u^s(\tilde{x}) = 0$$

in  $\tilde{\Omega}^b$ , where  $\tilde{\Delta} = \partial_{\tilde{x}_1}^2 + \partial_{\tilde{x}_2}^2$ . Defining the complexified function  $\tilde{u}^s(x) = u^s(\tilde{x})$  on  $\Omega^b$ , we see that equation (22) can be rewritten by the chain rule as

$$(23) \quad \nabla \cdot (\mathbf{A} \nabla \tilde{u}^s) + k_0^2 n^2 J \tilde{u}^s = 0,$$

where  $\alpha_1(x_1) = 1 + i\sigma_1(x_1)$ ,  $\alpha_2(x_2) = 1 + i\sigma_2(x_2)$ ,  $\mathbf{A} = \text{diag}\{\alpha_2/\alpha_1, \alpha_1/\alpha_2\}$ , and  $J(x) = \alpha_1(x_1)\alpha_2(x_2)$ .

As shown in [21, Theorem 2.8], the fundamental solution to (23), which we call the PML-transformed free-space Green's function, is

$$(24) \quad \tilde{G}(x, y) = G(\tilde{x}, \tilde{y}) = \frac{i}{4} H_0^{(1)}(k_0 n \rho(\tilde{x}, \tilde{y})),$$

where the complexified distance function  $\rho$  is defined to be

$$(25) \quad \rho(\tilde{x}, \tilde{y}) = [(\tilde{x}_1 - \tilde{y}_1)^2 + (\tilde{x}_2 - \tilde{y}_2)^2]^{1/2}$$

and the half-power operator  $z^{1/2}$  is chosen to be the branch of  $\sqrt{z}$  with nonnegative real part for  $z \in \mathbb{C} \setminus (-\infty, 0]$ . Then we have the following proposition.

PROPOSITION 3.2. *Let  $g \in H^{-1/2+\delta}(\Gamma^b)$  for  $0 < \delta < 1/2$ . If  $\tilde{u}^s \in H^{1+\delta}(\Omega^b)$  solves*

$$(26) \quad \begin{cases} \nabla \cdot (\mathbf{A} \nabla \tilde{u}^s) + k_0^2 n^2 J \tilde{u}^s = 0 & \text{in } \Omega^b, \\ \partial_{\nu_c} \tilde{u}^s = g & \text{on } \Gamma^b, \end{cases}$$

where  $\nu_c = \mathbf{A}^T \nu$  and  $\partial_{\nu_c} = \nu_c \cdot \nabla$ , then the trace  $\tilde{u}^s|_{\Gamma^b} \in H^{1/2+\delta}(\Gamma^b)$  and  $\partial_{\nu_c} \tilde{u}^s|_{\Gamma^b} \in H^{-1/2+\delta}(\Gamma^b)$  satisfy the integral representation

$$(27) \quad \tilde{u}^s(x) = \int_{\Gamma^b} \left\{ \tilde{G}(x, y) \partial_{\nu_c} \tilde{u}^s(y) - \partial_{\nu_c} \tilde{G}(x, y) \tilde{u}^s(y) \right\} ds(y)$$

for all  $x \in \Omega^b$ . Moreover, as  $x$  approaches  $\Gamma^b$ ,

$$(28) \quad (\tilde{\mathcal{K}} + \mathcal{I})(\tilde{u}^s)(x) = \tilde{\mathcal{S}}(\partial_{\nu_c} \tilde{u}^s)(x)$$

for a.e.  $x \in \Gamma^b$ . Here, the integral operators  $\tilde{\mathcal{S}}$  and  $\tilde{\mathcal{K}}$  are defined by (12) and (13) with  $G$  replaced by  $\tilde{G}$  and  $\nu$  replaced by  $\nu_c$ , respectively.

*Proof.* The proof is the same as Proposition 3.1(a) since the complexified Helmholtz equation in (26) is still strongly elliptic.  $\square$

Like equation (11), equation (28) should also be modified at corners. In fact, we have

$$(29) \quad \tilde{\mathcal{K}}(\tilde{u}^s)(x) - \tilde{\mathcal{K}}_0(1)\tilde{u}^s(x) = \tilde{\mathcal{S}}(\partial_{\nu_c}\tilde{u}^s)(x)$$

for all  $x \in \Gamma^b$ , where  $\tilde{\mathcal{K}}_0$  is defined as  $\tilde{\mathcal{K}}$  but with  $\tilde{G}(x, y)$  replaced by

$$(30) \quad \tilde{G}_0(x, y) = -\frac{1}{2\pi} \log \rho(\tilde{x}, \tilde{y}),$$

which is Green's function of the complexified Laplace equation

$$(31) \quad \nabla \cdot (\mathbf{A}\nabla\tilde{u}_0(x)) = 0.$$

The derivation is as follows. Setting  $k_0 = 0$  and  $\tilde{u}^s = 1$  in (27) so that  $\tilde{G}$  is replaced by  $\tilde{G}_0$ , we obtain

$$(32) \quad 1 = \int_{\Gamma^b} \{-\partial_{\nu_c}\tilde{G}_0(x, y)\}ds(y).$$

Then (27)– $\tilde{u}^s(x) \times$  (32) gives

$$(33) \quad \begin{aligned} & \int_{\Gamma^b} \partial_{\nu_c}(\tilde{G} - \tilde{G}_0)(x, y)\tilde{u}^s(y)ds(y) + \int_{\Gamma^b} \partial_{\nu_c}\tilde{G}_0(x, y)(\tilde{u}^s(y) - \tilde{u}^s(x))ds(y) \\ &= \int_{\Gamma^b} \tilde{G}(x, y)\partial_{\nu_c}\tilde{u}^s(y)ds(y). \end{aligned}$$

Consequently, equation (29) follows from the fact that both

$$\partial_{\nu_c}(\tilde{G} - \tilde{G}_0)(x, y) \text{ and } \partial_{\nu_c}\tilde{G}_0(x, y)(\tilde{u}^s(y) - \tilde{u}^s(x))$$

are weakly singular. As for  $\tilde{\mathcal{K}}_0(1)$ , we have exactly the same formula as (16) due to the following proposition.

PROPOSITION 3.3. *For any  $x \in \Gamma^b$ , we have*

$$(34) \quad \tilde{\mathcal{K}}_0(1)(x) = -\frac{\theta(x)}{\pi}.$$

*Proof.* At first, using Green's identity, we easily see that

$$(35) \quad \tilde{\mathcal{K}}_0(1)(x) = \lim_{r \rightarrow 0^+} 2 \int_{\partial B(x,r) \cap \overline{\Omega^b}} \partial_{\nu_c} G_0(x, y)ds(y),$$

where  $\partial B(x, r)$  is a circle of radius  $r$  centered at  $x$ , and here the unit normal vector  $\nu$  points toward  $\Omega^b$ .

For a sufficiently small  $r$ , one can parameterize  $\partial B(x, r) \cap \overline{\Omega^b}$  by  $y = x + r(\cos t, \sin t)$  for  $t \in [\theta_1, \theta_2]$  so that the interior angle  $\theta = \theta_2 - \theta_1$ . Thus, equation (35) becomes

$$(36) \quad \tilde{\mathcal{K}}_0(1)(x) = -\frac{1}{\pi} \lim_{r \rightarrow 0^+} \int_{\theta_1}^{\theta_2} \frac{(\tilde{y}_1 - \tilde{x}_1)\tilde{y}'_2 - \tilde{y}'_1(\tilde{y}_2 - \tilde{x}_2)}{|\tilde{x} - \tilde{y}|^2} dt.$$

By (18), we have

$$(37) \quad \tilde{y}_j - \tilde{x}_j = \int_{x_j}^{y_j} \alpha_j(s) ds = \int_{x_j}^{x_j+r \cos t} \alpha_j(s) ds = \alpha_j(x_j)r \cos t + O(r^2)$$

for  $j = 1, 2$ . Thus,

$$(38) \quad \begin{aligned} \tilde{\mathcal{K}}_0(1)(x) &= -\frac{1}{\pi} \lim_{r \rightarrow 0^+} \int_{\theta_1}^{\theta_2} \frac{\alpha_1(x_1)\alpha_2(x_2)r^2 + O(r^3)}{\alpha_1^2(x_1)r^2 \cos^2 t + \alpha_2^2(x_2)r^2 \sin^2 t + O(r^3)} dt \\ &= -\frac{1}{\pi} \int_{\theta_1}^{\theta_2} \frac{\alpha_1(x_1)\alpha_2(x_2)}{\alpha_1^2(x_1) \cos^2 t + \alpha_2^2(x_2) \sin^2 t} dt \\ &= -\frac{1}{\pi} \int_{\theta_1}^{\theta_2} d(\arctan(\alpha_2/\alpha_1 \tan t)). \end{aligned}$$

If  $x$  is outside the PML so that  $\alpha_1(x) = \alpha_2(x) = 1$ , then

$$\tilde{\mathcal{K}}_0(1)(x) = -\frac{\theta_2 - \theta_1}{\pi} = -\frac{\theta}{\pi}.$$

When  $x$  is inside the PML, one can easily verify (34) on each part of  $\Gamma^b$ . For example, if  $x$  is a smooth point of  $\Gamma_{AB}$ , then one sets  $\theta_1 = 0$  and  $\theta_2 = \pi$  so that  $\theta = \pi$ . Thus,

$$(39) \quad \tilde{\mathcal{K}}_0(1)(x) = -\frac{1}{\pi} \left( \int_0^{\pi/2} + \int_{\pi/2}^{\pi} d(\arctan(\alpha_2/\alpha_1 \tan t)) \right) = -\frac{\pi}{\pi}.$$

If  $x$  is at the vertex  $A$ , then one sets  $\theta_1 = 0$  and  $\theta_2 = \frac{\pi}{2}$  so that we obtain  $\tilde{\mathcal{K}}_0(1)(A) = -\frac{\pi/2}{\pi}$ , etc. □

In practice, through the use of equation (29), we define the PML-transformed NtD map as  $\tilde{\mathcal{N}} = (\tilde{\mathcal{K}} - \tilde{\mathcal{K}}_0(1))^{-1}\tilde{\mathcal{S}}$ , which maps  $\partial_{\nu_c} \tilde{u}^s$  to  $\tilde{u}^s$  on  $\Gamma^b$ ; the invertibility of  $\tilde{\mathcal{K}} - \tilde{\mathcal{K}}_0(1)$  is under investigation. Analogous to  $\mathcal{K}_0(1)$ , we need to numerically evaluate  $\tilde{\mathcal{K}}_0(1)$ .

**3.3. Truncation of  $\tilde{\mathcal{N}}$  onto  $\Gamma_{AB}$ .** According to the radiation condition,  $u^s$  is a superposition of outgoing plane waves and evanescent waves, but any outgoing plane wave becomes evanescent in the PML so that  $\tilde{u}^s$  in the PML becomes a superposition of evanescent waves only. Thus, we expect that  $\tilde{u}^s$  and  $\partial_{\nu_c} \tilde{u}^s$  decay to zero more rapidly than  $u^s$  and  $\partial_{\nu} u^s$  so that it is more accurate to approximate  $\tilde{u}^s \approx 0$  and  $\partial_{\nu_c} \tilde{u}^s \approx 0$  on  $\Gamma^+$ . Therefore, operators  $\tilde{\mathcal{K}}$  and  $\tilde{\mathcal{S}}$  in (28) can be truncated onto the truncated interface  $\Gamma_{AB}$  only; in other words,

$$(40) \quad \tilde{\mathcal{K}}_{AB}(\tilde{u}^s)(x) - \tilde{\mathcal{K}}_0(1)(x)\tilde{u}^s(x) \approx \tilde{\mathcal{S}}_{AB}(\partial_{\nu_c} \tilde{u}^s)(x)$$

for  $x \in \Gamma_{AB}$ , where the definition of  $\tilde{\mathcal{S}}_{AB}$  is the same as  $\tilde{\mathcal{S}}$  but with the integral domain replaced by  $\Gamma_{AB}$ , etc.

As for  $\tilde{\mathcal{K}}_0(1)$ , we need to remove the integration domain  $\Gamma^+$  so that only  $\Gamma_{AB}$  is involved. According to [22, section 8], one easily verifies that if  $x$  is neither  $A$  nor  $B$ , then

$$(41) \quad \tilde{\mathcal{K}}_0(1)(x) = \mathcal{K}_0(1)(x) = -\angle Ax B / \pi + \mathcal{K}_{0,AB}(1)(x),$$

where  $\angle AxB$  denotes the angle between and above the two segments  $Ax$  and  $xB$  (see Figure 2(b)) and  $\mathcal{K}_{0,AB}$  is defined by (14) but with the integration domain replaced by  $\Gamma_{AB}$ ; otherwise, we simply set  $\tilde{\mathcal{K}}_0(1)(x) = -1$ . Therefore, equation (40) becomes

$$(42) \quad \tilde{\mathcal{K}}_{AB}(\tilde{u}^s)(x) + (\angle AxB/\pi - \mathcal{K}_{0,AB}(1)(x)) \tilde{u}^s(x) \approx \tilde{\mathcal{S}}_{AB}(\partial_{\nu_c} \tilde{u}^s)(x).$$

Consequently, numerically discretizing the involved integral operators in (42) approximates the PML-transformed NtD map  $\tilde{\mathcal{N}}$  on  $\Gamma_{AB}$ .

**4. Numerical implementation.** In this section, we consider the discretization of the integral operators  $\tilde{\mathcal{K}}_{AB}$ ,  $\tilde{\mathcal{S}}_{AB}$ , and  $\mathcal{K}_{0,AB}$  on  $\Gamma_{AB}$ . Suppose the piecewise smooth curve  $\Gamma_{AB}$  is parameterized by  $x(s) = \{(x_1(s), x_2(s)) | 0 \leq s \leq L\}$ , where  $s$  is the arclength parameter. Since corners may exist,  $\tilde{u}^s$  can have corner singularities in its derivatives at corners. To treat the corner singularities of  $\tilde{u}^s$ , we follow [13, section 3.5], constructing a graded mesh on  $\Gamma_{AB}$  through the use of a scaling function  $s = w(t), 0 \leq t \leq 1$  so that integrands in (42) vanish at corners up to a certain order. For a smooth segment of  $\Gamma_{AB}$  corresponding to  $s \in [s^0, s^1]$  and  $t \in [t^0, t^1]$  such that  $s^l = w(t^l)$  for  $l = 0, 1$ , where  $s^0$  and  $s^1$  correspond to two corners, we take [13, equation (3.104)]

$$(43) \quad s = w(t) = \frac{s^0 w_1^p + s^1 w_2^p}{w_1^p + w_2^p}, \quad t \in [t^0, t^1],$$

where we recall that  $p$  is used in (20) to define  $\sigma_1$ , and

$$w_1 = \left(\frac{1}{2} - \frac{1}{p}\right) \xi^3 + \frac{\xi}{p} + \frac{1}{2}, \quad w_2 = 1 - w_1, \quad \xi = \frac{2t - (t^0 + t^1)}{t^1 - t^0}.$$

One easily verifies that the derivatives of  $w(t)$  vanish at the corners up to order  $p$ . Assume that  $t \in [0, 1]$  is uniformly sampled by an even number, denoted by  $N$ , of grid points  $\{t_j = jh\}_{j=1}^N$  with grid size  $h = 1/N$ , and that the grid points contain those corner points. The scaling function  $s = w(t)$  creates a graded mesh on  $\Gamma_{AB}$  such that roughly half the grid points cluster around the corners, whereas the other half are nearly equally distributed [13, section 3.5].

To simplify the notations, we use  $x(t)$  to denote  $x(w(t))$  and  $x'(t)$  to denote  $\frac{dx}{ds}(w(t))w'(t)$  in the following.

**4.1. Approximating  $\tilde{\mathcal{N}}$  on  $\Gamma_{AB}$ .** According to the definitions, operators  $\tilde{\mathcal{S}}_{AB}$  and  $\tilde{\mathcal{K}}_{AB}$  at  $x = x(t_l), l = 1, \dots, N$  can be parameterized by

$$(44) \quad \tilde{\mathcal{S}}_{AB}(\partial_{\nu_c} \tilde{u}^s)(x(t_l)) = \int_0^1 \tilde{S}(t_l, t) \phi(t) dt$$

$$(45) \quad \tilde{\mathcal{K}}_{AB}(\tilde{u}^s)(x(t_l)) = \int_0^1 \tilde{K}(t_l, t) \tilde{u}^s(x(t)) dt$$

where  $\phi(t) = \partial_{\nu_c} \tilde{u}^s(x(t)) |x'(t)|$ ,  $\text{dist}(t_l, t) = \rho(x(t_l), x(t))$ ,  $\kappa(t_l, t) = \tilde{x}'_2(t)(\tilde{x}_1(t) - \tilde{x}_1(t_l)) - \tilde{x}'_1(t)(\tilde{x}_2(t) - \tilde{x}_2(t_l))$ , and

$$(46) \quad \tilde{S}(t_l, t) = \frac{i}{2} H_0^{(1)}(k_0 n \text{dist}(t_l, t))$$

$$(47) \quad \tilde{K}(t_l, t) = -\frac{ik_0 n}{2} \frac{\kappa(t_l, t)}{\text{dist}(t_l, t)} H_1^{(1)}(k_0 n \text{dist}(t_l, t)).$$

TABLE 1  
Parameters for the sixth-order Alpert's quadrature rule.

| $k$ | $\delta_k$               | $\gamma_k$               |
|-----|--------------------------|--------------------------|
| 1   | 4.00488 41949 26570 E-03 | 1.67187 96911 47102 E-02 |
| 2   | 7.74565 53733 36686 E-02 | 1.63695 83714 47360 E-01 |
| 3   | 3.97284 99935 23248 E-01 | 4.98185 65697 70637 E-01 |
| 4   | 1.07567 33529 15104 E+00 | 8.37226 62455 78912 E-01 |
| 5   | 2.00379 69271 11872 E+00 | 9.84173 08440 88381 E-01 |

The integrands in (44) and (45) have logarithmic singularities at  $t = t_l$ . To discretize such integrals, a common approach is to use the kernel splitting technique introduced in [13, section 3.5], but this fails here. Taking  $\tilde{S}_{AB}$  as an example, this technique requires the decomposition

$$\tilde{S}(t_l, t) = \tilde{S}_1(t_l, t) \log(4 \sin^2(\pi(t_l - t))) + \tilde{S}_2(t_l, t),$$

where

$$(48) \quad \tilde{S}_1(t_l, t) = -\frac{1}{2\pi} J_0(k_0 n \operatorname{dist}(t_l, t))$$

and  $\tilde{S}_2$  are analytic for  $t \in [0, 1]$ . In the PML region, the Bessel function  $J_0$  blows up quickly toward infinity since  $\operatorname{dist}(t_l, t)$  is no longer real and may have a significant imaginary part.

Nevertheless, this can be simply remedied by Alpert's hybrid Gauss-trapezoidal quadrature rule [1], which does not perform kernel splittings. Following this approach, we discretize the integral in (44) as

$$(49) \quad \begin{aligned} \tilde{S}_{AB}(\partial_{\nu_c} \tilde{u}^s)(x(t_l)) \approx & \sum_{k=1}^{K_1} \gamma_k h \left[ \tilde{S}(t_l, t_l + \delta_k h) \phi(t_l + \delta_k h) \right. \\ & \left. + \tilde{S}(t_l, t_l + 1 - \delta_k h) \phi(t_l + 1 - \delta_k h) \right] \\ & + \sum_{k=K_2}^{N-K_2} h \tilde{S}(t_l, t_l + t_k) \phi(t_l + t_k), \end{aligned}$$

where values of  $K_1$ ,  $K_2$ ,  $\gamma_k$ , and  $\delta_k$  depend on the order of Alpert's quadrature rule and can be precomputed. For example, in a sixth-order quadrature formula, we have  $K_1 = 5$  and  $K_2 = 3$ ; the associated  $\{\delta_k, \gamma_k\}_{k=1}^5$  are given in Table 1 (see [1] for details).

By choosing a sufficiently large  $p$ , the scaling function  $w(t)$  can make the derivatives of  $\phi(t)$  vanish at the corners up to any given order so that  $\phi(t)$  is approximately a smooth periodic function. Therefore, its trigonometric interpolation [38, equation (3.8), Theorem 4.1] can be used to approximate  $\phi$  and attains a high accuracy. Thus, we have

$$(50) \quad \phi(t) \approx \sum_{j=1}^N \phi(t_j) L(t - t_j),$$

where  $L(t) = \sin(N\pi t)/[N \tan(\pi t)]$  is the Sinc function, satisfying  $L(t_j) = 0$  for  $1 \leq j < N$  and  $L(1) = L(0) = 1$ . Utilizing (50), we may rewrite equation (49) in terms of  $\phi(t_j)$  for  $1 \leq j \leq N$  so that we obtain an  $N \times N$  matrix  $\tilde{\mathbf{S}}$  that satisfies

$$(51) \quad \tilde{\mathcal{S}}_{AB}(\partial_{\nu_c} \tilde{u}^s) \begin{bmatrix} x(t_1) \\ \vdots \\ x(t_N) \end{bmatrix} \approx \tilde{\mathbf{S}} \begin{bmatrix} \phi(t_1) \\ \vdots \\ \phi(t_N) \end{bmatrix},$$

where the term on the left-hand side represents a column vector of  $\tilde{\mathcal{S}}_{AB}(\partial_{\nu_c} \tilde{u}^s)(x(t_j))$  for  $1 \leq j \leq N$ .

Similarly, one obtains the discretization of  $\tilde{\mathcal{K}}_{AB}$  as follows:

$$(52) \quad \tilde{\mathcal{K}}_{AB}(\tilde{u}^s) \begin{bmatrix} x(t_1) \\ \vdots \\ x(t_N) \end{bmatrix} \approx \tilde{\mathbf{K}} \begin{bmatrix} \tilde{u}^s(t_1) \\ \vdots \\ \tilde{u}^s(t_N) \end{bmatrix},$$

where  $\tilde{\mathbf{K}}$  represents an  $N \times N$  matrix, and so does the discretization of  $\mathcal{K}_{0,AB}$ .

Thus, collocating (42) at  $x(t_l), l = 1, \dots, N$ , yields

$$(53) \quad (\tilde{\mathbf{K}} + \tilde{\mathbf{H}})\tilde{\mathbf{u}}^s \approx \tilde{\mathbf{S}}\boldsymbol{\phi},$$

where  $\tilde{\mathbf{H}}$  is a diagonal matrix with entries  $\angle Ax(t_l)B/\pi - \mathcal{K}_{0,AB}(1)(x(t_l))$ ,

$$\begin{aligned} \tilde{\mathbf{u}}^s &= [\tilde{u}^s(x(t_1)), \dots, \tilde{u}^s(x(t_N))]^T, \\ \boldsymbol{\phi} &= [\phi(x(t_1)), \dots, \phi(x(t_N))]^T. \end{aligned}$$

Consequently, one gets

$$(54) \quad \tilde{\mathbf{u}}^s \approx (\tilde{\mathbf{K}} + \tilde{\mathbf{H}})^{-1} \tilde{\mathbf{S}}\boldsymbol{\phi} := \tilde{\mathbf{N}}\boldsymbol{\phi},$$

where the  $N \times N$  matrix  $\tilde{\mathbf{N}}$  in fact approximates the scaled PML-transformed NtD map  $\tilde{\mathcal{N}}_s$  mapping  $\boldsymbol{\phi} = |x'| \partial_{\nu_c} \tilde{u}^s$  to  $\tilde{u}^s$  on  $\Gamma_{AB}$ .

**4.2. A stabilizing technique.** Clearly, to make the approximations of  $\tilde{\mathcal{S}}_{AB}$  and  $\tilde{\mathcal{K}}_{AB}$  accurate enough, a high-order quadrature rule and a large scaling parameter  $p$  are always preferred; otherwise, one needs a large  $N$ . Suppose we desire sixth-order of accuracy so that nodes and weights of Alpert's quadrature rule are chosen based on Table 1. To be consistent, we choose  $p = 6$  in the scaling function  $s = w(t)$ . Under such a circumstance, when computing the kernel functions  $\tilde{S}(t_l, t)$  and  $\tilde{K}(t_l, t)$ , we observe that  $|t_l - t|$  can be as small as  $\delta_1 h = O(\frac{10^{-3}}{N})$ . When  $t_l$  is close to a corner point, the physical distance  $\text{dist}(t_l, t)$  can be further shrunk to  $O(\frac{10^{-3p}}{N^p}) = O(\frac{10^{-18}}{N^6})$  by  $s = w(t)$ . Unfortunately, even for a coarse mesh, this can be less than or close to the round-off error  $O(10^{-16}x(t_l))$  in the computation of  $\text{dist}(t_l, t)$ . In such a situation,  $\text{dist}(t_l, t)$  is simply regarded as 0 in a double-precision computation. Consequently, division by zero occurs in the computation of  $\tilde{S}(t_l, t)$  and  $\tilde{K}(t_l, t)$  when  $t$  is close to  $t_l$  and when  $t_l$  is close to a corner. To resolve this instability issue, one approach is to reduce  $p$  to be no more than 3, but this lowers the order of accuracy. Consequently, we develop a stabilizing technique which can provide sufficient significant digits in computing  $\tilde{S}(t_l, t)$  and  $\tilde{K}(t_l, t)$  in the extreme situation that  $t$  is close to  $t_l$ ,  $t_l$  is close to some corner, and  $p$  is high.

Observing the definitions (46) and (47), the instability issue comes from the two terms  $\text{dist}(t_l, t)$  and  $\kappa(t_l, t)$  since they involve subtractions of two extremely close quantities. We discuss  $\text{dist}(t_l, t)$  first. Without loss of generality, we assume that  $t > t_l$  so that  $\tilde{x}(\xi)$  for  $\xi \in [t_l, t]$  becomes a piecewise smooth function; note that here

$\tilde{x}(\xi)$  may contain the corner. At first, we assume that  $\tilde{x}(\xi)$  for  $\xi \in [t_l, t]$  is smooth. To preserve enough significant digits, we compute accurately

$$(55) \quad \tilde{x}_i(t) - \tilde{x}_i(t_l)$$

for  $i = 1, 2$ . To do so, by the Newton–Leibniz formula, we rewrite (55) in the form

$$(56) \quad \tilde{x}_i(t) - \tilde{x}_i(t_l) = \int_0^{\int_{t_l}^t w'(\tau) d\tau} \frac{d\tilde{x}_i}{ds}(w(t_l) + s) ds$$

for  $i = 1, 2$ . Such a representation gives rise to significant advantages. Specifically, the integrand in the primary integral is an  $O(1)$  quantity so that numerical integrations (e.g., Gaussian quadrature rules) yield accurate results; moreover, we only need the first-order derivative of  $\tilde{x}_i$  to obtain accurate results. Consequently,  $\text{dist}(t_l, t)$  can be evaluated via

$$(57) \quad \text{dist}(t_l, t) = \sqrt{\sum_{i=1}^2 \left( \int_0^{\int_{t_l}^t w'(\tau) d\tau} \frac{d\tilde{x}_i}{ds}(w(t_l) + s) ds \right)^2}.$$

Next, we discuss the computation of

$$(58) \quad \begin{aligned} \kappa(t_l, t) &= w'(t) \left[ \frac{d\tilde{x}_2}{ds}(w(t)) (\tilde{x}_1(w(t)) - \tilde{x}_1(w(t_l))) \right. \\ &\quad \left. - \frac{d\tilde{x}_1}{ds}(w(t)) (\tilde{x}_2(w(t)) - \tilde{x}_2(w(t_l))) \right] \\ &:= w'(t) \bar{\kappa}(t_l, t). \end{aligned}$$

Using the Newton–Leibniz formula, we may rewrite  $\bar{\kappa}(t_l, t)$  as

$$(59) \quad \begin{aligned} \bar{\kappa}(t_l, t) &= \int_0^{\int_{t_l}^t w'(\tau) d\tau} \int_0^s \left[ \frac{d^2\tilde{x}_2}{ds^2}(w(t_l) + s) \frac{d\tilde{x}_1}{ds}(w(t_l) + \eta) \right. \\ &\quad \left. - \frac{d^2\tilde{x}_1}{ds^2}(w(t_l) + s) \frac{d\tilde{x}_2}{ds}(w(t_l) + \eta) \right] d\eta ds. \end{aligned}$$

Numerical integrations for the above double integrals provide accurate results.

Now suppose that  $\tilde{x}(\xi)$  for  $\xi \in [t_l, t]$  contains a corner at  $t^* \in (t_l, t)$ . Since  $\tilde{x}(\xi)$  consists of two smooth segments corresponding to  $[t_l, t^*]$  and  $[t^*, t]$ , respectively, the splitting

$$(60) \quad \tilde{x}_i(t) - \tilde{x}_i(t_l) = (\tilde{x}_i(t) - \tilde{x}_i(t^*)) + (\tilde{x}_i(t^*) - \tilde{x}_i(t_l))$$

indicates that the Newton–Leibniz formula is applicable to either term on the right-hand side so that numerical integrations lead to accurate results for  $\tilde{x}_i(t) - \tilde{x}_i(t_l)$  and for  $\text{dist}(t_l, t)$ . One may compute  $\kappa(t_l, t)$  similarly; we omit the details here.

**4.3. Wave field evaluations.** Suppose now in each domain  $\Omega_j$  that we have obtained an  $N \times N$  matrices  $\tilde{\mathbf{N}}_j$  to approximate the scaled NtD operator  $\tilde{\mathcal{N}}_{s,j}$ , mapping  $|x'\rangle \partial_{\nu_c} \tilde{u}_j^s$  to  $\tilde{u}_j^s$  on  $\Gamma_{AB}$  for  $j = 1, 2$ . Then

$$(61) \quad \tilde{\mathbf{N}}_j \phi_j = \tilde{\mathbf{u}}_j^s,$$

where

$$\begin{aligned}\tilde{\mathbf{u}}_j^s &= [\tilde{u}_j^s(x(t_1)), \dots, \tilde{u}_j^s(x(t_N))]^T, \\ \phi_j &= [|x'(t_1)|\partial_{\nu_c}\tilde{u}_j^s(x(t_1)), \dots, |x'(t_N)|\partial_{\nu_c}\tilde{u}_j^s(x(t_N))]^T.\end{aligned}$$

According to the transmission conditions (6) and (7), the complexified outgoing wave  $\tilde{u}_j^s$ , at the  $N$  grid points on  $\Gamma_{AB}$ , satisfies

$$(62) \quad \tilde{\mathbf{u}}_1^s - \tilde{\mathbf{u}}_2^s = \mathbf{b}_1$$

$$(63) \quad \eta_1\phi_1 - \eta_2\phi_2 = \mathbf{b}_2$$

where

$$\begin{aligned}\mathbf{b}_1 &= [-[\tilde{u}_0^{tot}](x(t_1)), \dots, -[\tilde{u}_0^{tot}](x(t_N))]^T, \\ \mathbf{b}_2 &= [-|x'(t_1)|[\eta_j\partial_{\nu_c}\tilde{u}_0^{tot}](x(t_1)), \dots, -|x'(t_N)|[\eta_j\partial_{\nu_c}\tilde{u}_0^{tot}](x(t_N))]^T.\end{aligned}$$

Thus, by (61), we obtain

$$(64) \quad \begin{bmatrix} \tilde{\mathbf{N}}_1 & -\tilde{\mathbf{N}}_2 \\ \eta_1\mathbf{I} & -\eta_2\mathbf{I} \end{bmatrix} \begin{bmatrix} \phi_1 \\ \phi_2 \end{bmatrix} = \begin{bmatrix} \mathbf{b}_1 \\ \mathbf{b}_2 \end{bmatrix}$$

with the solution

$$(65) \quad \phi_1 = \left( \tilde{\mathbf{N}}_1 - \frac{\eta_1}{\eta_2}\tilde{\mathbf{N}}_2 \right)^{-1} \left( \eta_2^{-1}\tilde{\mathbf{N}}_2\mathbf{b}_2 + \mathbf{b}_1 \right)$$

$$(66) \quad \phi_2 = \frac{\eta_1}{\eta_2}\phi_1 - \frac{\mathbf{b}_2}{\eta_2}.$$

Consequently, we obtain  $\tilde{\mathbf{u}}_j^s = \tilde{\mathbf{N}}_j\phi_j$  on  $\Gamma_{AB}$ .

As for  $x \in \Omega_j$ , we directly truncate the integration domain in (27) to  $\Gamma_{AB}$  to compute  $\tilde{u}_j^s(x)$ ; that is,

$$(67) \quad \tilde{u}_j^s(x) \approx \int_{\Gamma_{AB}} \{ \tilde{G}_j(x, y)\partial_{\nu_c}\tilde{u}_j^s(y) - \partial_{\nu_c}\tilde{G}_j(x, y)\tilde{u}_j^s(y) \} ds(y).$$

After parameterized by the scaling function  $s = w(t)$  in (43), the integrand in (67) becomes periodic and smooth enough so that by the trapezoidal rule, we have

$$(68) \quad \tilde{u}_j^s(x) \approx \frac{1}{N} \sum_{l=1}^N \left[ \tilde{G}_j(x, x(t_l))|x'(t_l)|\partial_{\nu_c}\tilde{u}_j^s(x(t_l)) - \partial_{\nu_c}\tilde{G}_j^s(x, x(t_l))|x'(t_l)|\tilde{u}_j^s(x(t_l)) \right].$$

Therefore, we obtain  $u_j^s = \tilde{u}_j^s$  so that the total wave field  $u^{tot} = u^s + u_0^{tot}$  in the physical domain outside the PML.

**5. Numerical examples.** In this section, we will carry out several numerical experiments to demonstrate the efficiency of the proposed PML-BIE formulation. In all examples, the physical domain  $\Omega_{\text{PHY}} = \{(x_1, x_2) | |x_1| \leq a_1\}$  where we let  $a_2$  in (19) approach infinity since the choice of  $a_2$  does not affect computing  $\tilde{u}_j^s$  on  $\Gamma_{AB}$  for  $j = 1, 2$ . Accordingly, the PML domain  $\Omega_{\text{PML}} = \{(x_1, x_2) | a_1 \leq |x_1| \leq a_1 + T, a_1 > 0, T > 0\}$ . Therefore, the truncated interface  $\Gamma_{AB}$  consists of physical interface  $\Gamma_{\text{PHY}} = \overline{\Omega_{\text{PHY}}} \cap \Gamma_{AB}$  and the PML interface  $\Gamma_{\text{PML}} = \overline{\Omega_{\text{PML}}} \cap \Gamma_{AB}$ .

To achieve a high-order accuracy, we take  $p = 6$  to define  $\sigma_1$  and the scaling function  $w(t)$ , and we apply the sixth-order Alpert’s quadrature rule with parameters defined in Table 1 to discretize the governing BIEs. In all examples, we will take the free-space wavelength  $\lambda = 1$  so that  $k_0 = 2\pi$ , and we will fix the PML thickness  $T = \lambda$ .

The truncation error induced in (40) depends on how rapidly  $\tilde{u}^s$  decays in the PML, especially along the  $x_1$ -axis, and this in fact can be controlled by adjusting  $\sigma_1$  in the PML [12]. By (20),  $\sigma_1$  is proportional to its parameter  $S$  so that we expect that the truncation error can be suppressed by increasing  $S$ ; we will see below that for PMLs with a thickness of one wavelength, one can get sufficiently accurate solutions by choosing  $S = 2$ .

*Example 5.1.* In this example, we assume that  $\Gamma$  is just the flat interface  $x_2 = 0$ . We take  $n_1 = 1$  and  $n_2 = 2$  and study a cylindrical incident wave excited by the source  $x^* = (0, 0.1)$  so that  $u^{tot}$  represents the layered Green’s function at  $x^*$ . This example is used to validate our method since a closed form of the layered Green’s function is available [31].

In the implementation, although  $\Gamma$  is smooth, we set  $(0, 0) \in \Gamma$  as an artificial corner. The reason is that the solution can change extremely rapidly at  $(0, 0)$  since it is the closest point to the source  $x^*$  on  $\Gamma$ . To capture this sharply changing behavior, we need more points near  $(0, 0)$ , and regarding  $(0, 0)$  as an artificial corner is a quick way to realize the purpose. We consider the TM polarization here and take  $a_2 = a_1 = 1$  so that  $\Omega_{\text{PHY}} = [-1, 1] \times [-1, 1]$ .

Taking  $N = 400$ , we compute  $\tilde{u}^{tot}$  and compare it with the exact solution  $u_{exa}^{tot}$  on  $\Gamma_{AB}$ , as shown in Figure 4(a), where the dashed lines are used to separate  $\Gamma_{\text{PML}}$  and  $\Gamma_{\text{PHY}}$ . We observe that on  $\Gamma_{\text{PHY}}$ ,  $\tilde{u}^{tot} = u^{tot}$  and  $u_{exa}^{tot}$  coincide very well, whereas on  $\Gamma_{\text{PML}}$ ,  $\tilde{u}^{tot}$  decays quickly to 0 and  $u_{exa}^{tot}$  keeps oscillating, as we expected. Figure 4(b) and 4(c) shows the real part of numerical and exact solutions of  $u^{tot}$  in  $\Omega_{\text{PHY}}$ , respectively.

To illustrate that our PML effectively absorbs  $u^s$ , we fix  $N = 400$  and compute  $u^{tot}$  at grid points on  $\Gamma_{\text{PHY}}$  for different values of  $S$ , ranging from 0.1 to 2; notice that the grid points on  $\Gamma_{\text{PHY}}$  are independent of  $S$ . Using the exact solution  $u_{exa}^{tot}$  as a reference solution, we compute relative errors for different values of  $S$ , as shown in Figure 5(a), where only the vertical axis is logarithmically scaled. Those relative errors can somewhat measure the magnitude of the truncation error in (40). We observe that the relative error decays exponentially at the beginning and then yields to the discretization error, which dominates the total error when  $S$  becomes large.

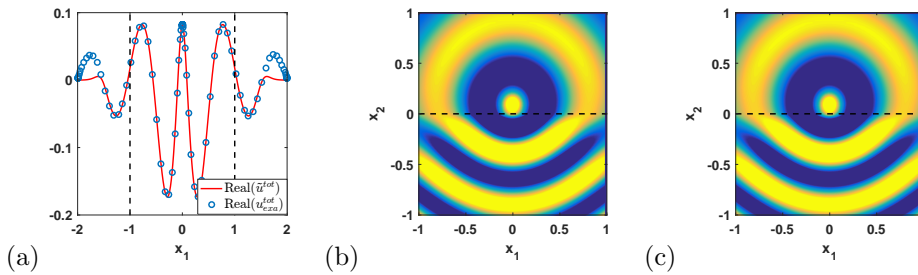


FIG. 4. *Example 5.1, in TM polarization: (a) real parts of  $\tilde{u}^{tot}$  and  $u_{exa}^{tot}$  on  $\Gamma_{AB}$ ; dashed lines separate  $\Gamma_{\text{PML}}$  and  $\Gamma_{\text{PHY}}$ . Real part of  $u^{tot}$  in  $\Omega_{\text{PHY}}$ : (b) numerical solution and (c) exact solution, where dashed lines represent location of  $\Gamma$ .*

Next, we study the relative error of  $u^{tot}$  on  $\Gamma_{PHY}$ , varying the number of grid points  $N$  on  $\Gamma_{AB}$  for  $S = 2$ . Since grid points vary for different values of  $N$ , to realize the comparison, we choose to evaluate  $u^{tot}$  at the following observation points: the grid points on  $\Gamma_{PHY}$  for  $N = 20$ ; for  $N$  greater than 20, we interpolate the numerical solution onto the observation points by (50). Relative errors for different values of  $N$  are depicted in Figure 5(b) with both axes logarithmically scaled. The slope of the decreasing part of the curve reveals that our method exhibits at least seventh-order accuracy.

*Example 5.2.* We next consider a local perturbation that consists of two connected semicircles of radius 1; the interface is shown as dashed lines in Figure 6(a) and 6(b). Suppose  $n_1 = 1$  and  $n_2 = 2$ . We consider two different incident waves: a plane wave with the incident angle  $\alpha = \frac{\pi}{3}$  and a cylindrical wave excited by the source  $x^* = (1, 1)$ .

In the implementation, we consider the TE polarization and take  $a_2 = a_1 = 2.5$  so that  $\Omega_{PHY} = [-2.5, 2.5] \times [-2.5, 2.5]$ . The total wave field  $u^{tot}$  for two incident waves in  $\Omega_{PHY}$  is plotted in Figure 6(a) and 6(b), respectively.

Next, we fix  $N = 1600$  and compute  $u^{tot}$  at grid points on  $\Gamma_{PHY}$  for different values of  $S$ , ranging from 0.1 to 2. Taking the numerical solution  $u^{tot}$  for  $S = 2$  as a reference solution, we compute relative errors for different values of  $S$  for both incident waves. Numerical results are shown in Figure 6(c).

Finally, we study relative errors of  $u^{tot}$  on  $\Gamma_{PHY}$ , varying  $N$  for  $S = 2$ . Observation points are chosen as the grid points on  $\Gamma_{PHY}$  for  $N = 80$ . The reference solution is

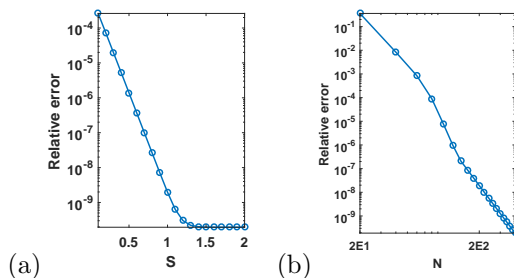


FIG. 5. *Example 5.1, in TM polarization:* (a) relative error against  $S$  for  $N = 400$  and (b) relative error against  $N$  for  $S = 2$ .

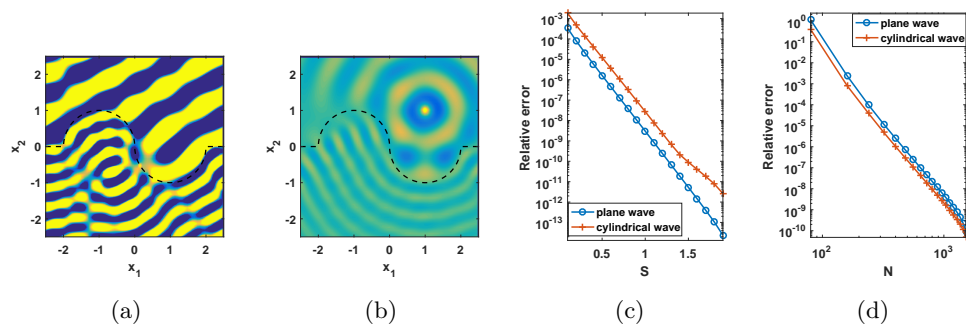


FIG. 6. *Example 5.2, in TE polarization, real part of the wave  $u^{tot}$  in  $\Omega_{PHY}$ :* (a) plane incident wave with angle  $\alpha = \frac{\pi}{3}$  and (b) cylindrical incident wave with source  $x^* = (1, 1)$ , where dashed lines indicate location of  $\Gamma$ . (c) relative error of  $u^{tot}$  on  $\Gamma_{PHY}$  against  $S$  for  $N = 1600$ . (d) relative error of  $u^{tot}$  on  $\Gamma_{PHY}$  against  $N$  for  $S = 2$ .

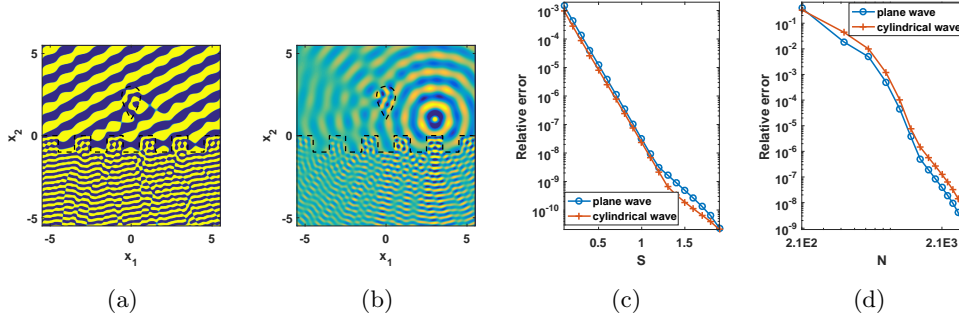


FIG. 7. Example 5.3, in TM polarization, real part of  $u^{tot}$  in  $\overline{\Omega_{\text{PHY}}}$ : (a) plane incident wave with angle  $\alpha = \frac{\pi}{3}$  and (b) cylindrical incident wave with point source  $x^* = (3, 1)$ , where dashed line indicates location of  $\Gamma$ . When  $N_{ob} = 800$ : (c) relative error of  $u^{tot}$  on  $\Gamma_P$  against  $S$  for  $N = 3150$ . (d) relative error of  $u^{tot}$  on  $\Gamma_P$  against  $N$  for  $S = 2$ .

obtained by interpolating the numerical solution for  $N = 1600$  onto the observation points. Numerical results for both incident waves are shown in Figure 6(d).

*Example 5.3.* In the third example, we study a more complicated structure, where an obstacle is placed above the interface. With the obstacle involved, our PML-based BIE formulation only requires an extra NtD operator defined on the boundary of the obstacle, which can be computed through the use of (17) [22]. Then, according to transmission conditions on the obstacle and the interface, the final linear system can be obtained by the same procedure.

Suppose  $n_1 = 1$ ,  $n_2 = 3$ , and the refractive index of the obstacle is  $n_{ob} = 2$ . The structure is shown in Figure 7, where the interface contains five uniformly spaced indentations and a drop-shaped obstacle is located one unit above the interface. We consider two different incident waves: a plane wave with the incident angle  $\alpha = \frac{\pi}{3}$  and a cylindrical wave excited by the source  $x^* = (3, 1)$ .

In the implementation, we consider the TM polarization and take  $a_2 = a_1 = 5.5$  so that  $\Omega_{\text{PHY}} = [-5.5, 5.5] \times [-5.5, 5.5]$ . The total wave field  $u^{tot}$  for two incident waves in  $\Omega_{\text{PHY}}$  is plotted in Figure 7(a) and 7(b), respectively.

Taking  $N = 3150$  and  $N_{ob} = 800$ , we next compute  $u^{tot}$  at grid points on  $\Gamma_{\text{PHY}}$  for  $S$  ranging from 0.1 to 2. Taking the numerical solution for  $S = 2$  as a reference solution, we compute relative errors for different values of  $S$  for both incident waves. Numerical results are shown in Figure 7(c).

Finally, we study numerical errors of  $u^{tot}$  on  $\Gamma_{\text{PHY}}$ , varying  $N$  when  $S = 2$  and  $N_{ob} = 800$ . Observation points are chosen as the grid points on  $\Gamma_{\text{PHY}}$  when  $N = 210$ . The reference solution is obtained by interpolating the numerical solution for  $N = 3150$  onto the observation points. Numerical results for both incident waves are shown in Figure 7(d).

**6. Conclusion.** For 2D scattering problems in layered media with unbounded interfaces, we developed a PML-based BIE method that relies on the PML-transformed free-space Green’s function, which is very easy to evaluate. The method avoids the difficulty of evaluating the expensive Sommerfeld integrals. Similar to other BIE methods based on the free-space Green’s function, integral equations are formulated on unbounded interfaces of the background media, and these interfaces must be truncated. Unlike existing truncating approaches, the truncation in our method simply follows the well-established PML technique.

Since our main purpose is to develop a PML-based method and demonstrate its effectiveness for truncating the unbounded interfaces, we have used a BIE formulation involving the single- and double-layer boundary integral operators only. In addition, we used the NtD maps to simplify the final linear system. Numerical examples are presented for scattering problems involving two homogeneous media separated by an interface with local perturbations and possibly with additional obstacles. The integral equations are discretized using a graded mesh technique, Alpert's sixth-order hybrid Gauss-trapezoidal rule for logarithmic singularities, and a stabilizing technique. Numerical results indicate that the truncation of interfaces by PML is highly effective. Using PMLs with one-wavelength thickness, we obtained at least seven significant digits in all experiments.

The PML-based BIE method can be extended in a number of directions. Obviously, the method can be used to study scattering problems in multilayered media with local perturbations, embedded obstacles, and penetrable structures. Besides scattering problems, the method can also be used to study eigenvalue problems, such as the problem for guided modes in open waveguide structures. We are planning to address these problems in our future works.

**Acknowledgments.** We thank the two anonymous referees for their helpful comments.

#### REFERENCES

- [1] B. K. ALPERT, *Hybrid Gauss-trapezoidal quadrature rules*, SIAM J. Sci. Comput., 20 (1999), pp. 1551–1584.
- [2] T. ARENS AND T. HOHAGE, *On radiation conditions for rough surface scattering problems*, SIAM J. Appl. Math., 70 (2005), pp. 839–847.
- [3] J.-P. BERENGER, *A perfectly matched layer for the absorption of electromagnetic waves*, J. Comput. Phys., 114 (1994), pp. 185–200.
- [4] O. P. BRUNO AND B. DELOURME, *Rapidly convergent two-dimensional quasi-periodic Green function throughout the spectrum including wood anomalies*, J. Comput. Phys., 262 (2014), pp. 262–290.
- [5] O. P. BRUNO, M. LYON, C. PÉREZ-ARANCIBIA, AND C. TURC, *Windowed Green function method for layered-media scattering*, SIAM J. Appl. Math., 76 (2016), pp. 1871–1898.
- [6] W. CAI, *Algorithmic issues for electromagnetic scattering in layered media: Green's functions, current basis, and fast solver*, Adv. Comput. Math., 16 (2002), pp. 157–174.
- [7] W. CAI, *Computational Methods for Electromagnetic Phenomena*, Cambridge University Press, New York, 2013.
- [8] W. CAI AND T. J. YU, *Fast calculations of dyadic Green's functions for electromagnetic scattering in a multilayered medium*, J. Comput. Phys., 5 (2000), pp. 247–251.
- [9] S. N. CHANDLER-WILDE AND B. ZHANG, *A uniqueness result for scattering by infinite rough surfaces*, SIAM J. Appl. Math., 58 (1998), pp. 1774–1790.
- [10] Z. CHEN AND X. XIANG, *A source transfer domain decomposition method for Helmholtz equations in unbounded domain*, SIAM J. Numer. Anal., 51 (2013), pp. 2331–2356.
- [11] W. C. CHEW, *Waves and Fields in Inhomogeneous Media*, IEEE Press, New York, 1995.
- [12] W. C. CHEW AND W. H. WEEDON, *A 3D perfectly matched medium for modified Maxwell's equations with stretched coordinates*, Microw. Opt. Technol. Lett., 7 (1994), pp. 599–604.
- [13] D. COLTON AND R. KRESS, *Inverse Acoustic and Electromagnetic Scattering Theory*, 3rd ed., Springer, New York, 2013.
- [14] T. J. CUI AND W. C. CHEW, *Efficient evaluation of Sommerfeld integrals for TM wave scattering by buried objects*, J. Electromagn. Waves Appl., 12 (1998), pp. 607–657.
- [15] T. J. CUI AND W. C. CHEW, *Fast evaluation of Sommerfeld integrals for EM scattering and radiation by three-dimensional buried objects*, IEEE Trans. Geosci. Remote Sensing, 37 (1999), pp. 887–900.
- [16] V. DOMINGUEZ, M. LYON, AND C. TURC, *Well-posed boundary integral equation formulations and Nyström discretizations for the solution of Helmholtz transmission problems in two-dimensional Lipschitz domains*, J. Integral Equations Appl., 28 (2016), pp. 395–440.

- [17] J. DeSANTO AND P. A. MARTIN, *On the derivation of boundary integral equations for scattering by an infinite one-dimensional rough surface*, J. Acoust. Soc. Amer., 102 (1997), pp. 67–77.
- [18] R. KRESS, *A Nyström method for boundary integral equations in domains with corners*, Numer. Math., 58 (1990), pp. 145–161.
- [19] R. KRESS, *Linear Integral Equations*, 3rd ed., Springer, New York, 2014.
- [20] J. LAI, L. GREENGARD, AND M. O'NEIL, *A New Hybrid Integral Representation for Frequency Domain Scattering in Layered Media*, preprint, arXiv:1507.04445v2, 2015.
- [21] M. LASSAS AND E. SOMERSALO, *Analysis of the PML equations in general convex geometry*, Proc. Roy. Soc. Edinburgh Sect. A, 131 (2001), pp. 1183–1207.
- [22] W. LU AND Y. Y. LU, *Efficient high order waveguide mode solvers based on boundary integral equations*, J. Comput. Phys., 272 (2014), pp. 507–525.
- [23] W. McLEAN, *Strongly Elliptic Systems and Boundary Integral Equations*, Cambridge University Press, Cambridge, 2000.
- [24] A. MEIER AND S. N. CHANDLER-WILDE, *On the stability and convergence of the finite section method for integral equation formulations of rough surface scattering*, Math. Methods Appl. Sci., 24 (2001), pp. 209–232.
- [25] D. MIRET, G. SORIANO, AND M. SAILLARD, *Rigorous simulations of microwave scattering from finite conductivity two-dimensional sea surfaces at low grazing angles*, IEEE Trans. Geosci. Remote Sensing, 52 (2014), pp. 3150–3158.
- [26] P. MONK, *Finite Element Methods for Maxwell's Equations*. Oxford University Press, Oxford, 2003.
- [27] J. A. MONRO, *A super-algebraically convergent, windowing-based approach to the evaluation of scattering from periodic rough surfaces*, Ph.D. dissertation, California Institute of Technology, Pasadena, CA, 2008.
- [28] M. OCHMANN, *The complex equivalent source method for sound propagation over an impedance plane*, J. Acoustical Soc. Amer., 116 (2004), pp. 3304–3311.
- [29] V. I. OKHMATOVSKI AND A. C. CANGELLARIS, *Evaluation of layered media Green's functions via rational function fitting*, IEEE Microw. Wirel. Components Lett., 14 (2004), pp. 22–24.
- [30] M. PAULUS, P. GAY-BALMAZ, AND O. J. F. MARTIN, *Accurate and efficient computation of the Green's tensor for stratified media*, Phys. Rev. E, 62 (2000), pp. 5797–5807.
- [31] C. PÉREZ-ARANCIBIA AND O. P. BRUNO, *High-order integral equation methods for problems of scattering by bumps and cavities on half-planes*, J. Opt. Soc. Amer. A, 31 (2014), pp. 1738–1746.
- [32] B. VAN D. POL, *Theory of the reflection of the light from a point source by a finitely conducting flat mirror, with an application to radiotelegraphy*, Physica, 2 (1935), pp. 843–853.
- [33] M. SAILLARD AND G. SORIANO, *Rough surface scattering at low-grazing incidence: A dedicated model*, Radio Sci., 46 (2011), pp. n/a–n/a. RS0E13.
- [34] A. SOMMERFELD, *Über die ausbreitung der wellen in der drahtlosen telegraphie*, Ann. Phys., 333 (1909), pp. 665–736.
- [35] P. SPIGA, G. SORIANO, AND M. SAILLARD, *Scattering of electromagnetic waves from rough surfaces: A boundary integral method for low-grazing angles*, IEEE Trans. Antennas Propagation, 56 (2008), pp. 2043–2050.
- [36] G. TARALDSEN, *The complex image method*, Wave Motion, 43 (2005), pp. 91–97.
- [37] D. J. THOMSON AND J. T. WEAVER, *The complex image approximation for induction in a multilayered earth*, J. Geophys. Res., 80 (1975), pp. 123–129.
- [38] L. N. TREFETHEN, *Spectral Methods in MATLAB*, SIAM, Philadelphia, PA, 2000.
- [39] H. WEYL, *Ausbreitung elektromagnetischer wellen ber einem ebenen leiter*, Ann. Phys., 365 (1919), pp. 481–500.
- [40] Z. ZHAO, L. LI, J. SMITH, AND L. CARIN, *Analysis of scattering from very large three-dimensional rough surfaces using mlfmm and ray-based analyses*, IEEE Antennas Propagation Mag., 47 (2005), pp. 20–30.